Neural Comput & Applic (2018) 30:3467–3478
DOI 10.1007/s00521-017-2933-8

ORIGINAL ARTICLE

Numerical study of radiative Maxwell viscoelastic magnetized flow from a stretching permeable sheet with the Cattaneo–Christov heat flux model

A. Shahid[1] · M. M. Bhatti[2] · O. Anwar Bég[3] · A. Kadir[4]

Received: 21 December 2016 / Accepted: 1 March 2017 / Published online: 9 March 2017

Abstract In this article, the Cattaneo–Christov heat flux model is implemented to study non-Fourier heat and mass transfer in the magnetohydrodynamic flow of an upper-convected Maxwell fluid over a permeable stretching sheet under a transverse constant magnetic field. Thermal radiation and chemical reaction effects are also considered. The nonlinear partial differential conservation equations for mass, momentum, energy and species conservation are transformed with appropriate similarity variables into a system of coupled, highly nonlinear ordinary differential equations with appropriate boundary conditions. Numerical solutions have been presented for the influence of elasticity parameter (α), magnetic parameter (M^2), suction/injection parameter (λ), Prandtl number (Pr), conduction–radiation parameter (R_d), sheet stretching parameter (A), Schmidt number (Sc), chemical reaction parameter (γ_c), modified Deborah number with respect to relaxation time of heat flux (i.e., non-Fourier Deborah number) on velocity components, temperature and concentration profiles using the successive Taylor series linearization method (STSLM) utilizing Chebyshev interpolating polynomials and Gauss–Lobatto collocation. The effects of selected parameters on skin friction coefficient, Nusselt number and Sherwood number are also presented with the help of tables. Verification of the STSLM solutions is achieved with existing published results demonstrating close agreement. Further validation of skin friction coefficient, Nusselt number and Sherwood number values computed with STSLM is included using Mathematica software shooting quadrature.

Keywords Heat and mass transfer · Magnetohydrodynamics · UC Maxwell viscoelastic fluid · Heat flux · Radiative flux · STSLM numerical solution

1 Introduction

Heat transfer is an important area of research due to its numerous applications in different industrial and engineering processes. These include cooling of nuclear reactors, thermoplastic fabrication, heat pumps, materials processing, cooling of electronic devices, biophysical heat conduction process in tissues, rocket thermal ablation and energy production. The Fourier law of heat conduction [1] has been the classical approach for thermal conduction heat transfer simulation. The main drawback of this model, however, is that it reduces the heat conservation formulation to a parabolic energy equation which shows that the medium under observation experiences an initial disturbance. In order to overcome this difficulty, Cattaneo [2] introduced a relaxation time term in Fourier's law of heat conduction. Christov [3] presented a frame indifferent formulation for the Maxwell–Cattaneo model with finite-speed heat conduction. Ostoja-Starzewski [4] described mathematically the Maxwell–Cattaneo equation with the help of a material time derivative for heat flux. Tibullo and Zampoli [5] investigated the uniqueness and stability of solutions obtained by the Cattaneo–Christov heat flux

✉ A. Shahid
aforshahid@gmail.com; 1111515014@e.gzhu.edu.cn

[1] School of Mathematics and Information Sciences, Guangzhou University, Guangzhou, China

[2] Shanghai Institute of Applied Mathematics and Mechanics, Shanghai University, Shanghai 200072, China

[3] Aeronautical & Mechanical Engineering Department, SCSE, University of Salford, Manchester M54WT, UK

[4] Petroleum and Gas Engineering Division, SCSE, University of Salford, Manchester M54WT, UK

model for incompressible fluid. Straughan [6] numerically examined incompressible thermal convection flows using the Cattaneo–Christov model. He found that thermal relaxation coefficient is more significant if the Cattaneo number is very high and the convection phenomena transform from stationary convection to oscillatory convection having narrower cells. A study of thermal instability incorporating fluid inertia using heat flux model through a Brinkman porous medium was conducted by Haddad [7]. Ciarletta and Straughan [8] addressed the structural uniqueness and stability of Cattaneo–Christov heat flux equations. They show that the solution to a backward in time problem relies on continuously on a relaxation time. Al-Qahtani and Yilbas [9] presented a closed form solution for Cattaneo and stress equation by means of the Laplace transform method. Papanicolaou et al. [10] examined the effects of thermal relaxation in the Cattaneo–Maxwell equations using horizontal and vertical gradients. Recently, Han et al. [11] studied the boundary layer flow of Maxwell fluids from a stretching sheet with the Cattaneo–Christov heat flux model. Mustafa [12] investigated analytically and numerically the non-Fourier convection in rotating Maxwell fluid flow. He presented both analytical and numerical solution and showed that both the results are in excellent agreement. Bissell [13] examined oscillatory convection flow using Cattaneo–Christov heat flux model in place of parabolic of parabolic Fourier law to enhance the possibility of oscillatory convection in a classic Bernard problem. Nadeem et al. [14] studied numerically the heat transfer in boundary layer flow of an Oldroyd-B nanofluid model toward a stretching sheet with a non-Fourier thermal flux model. They observed that the Brownian motion parameter enhances the Nusselt number and Sherwood number.

In recent year's, boundary layer flows of both Newtonian and non-Newtonian fluids have stimulated considerable attention in engineering science research owing to growing applications in metallurgical processing, chemical engineering transport phenomena (paints, gels, foodstuffs), extrusion of molten polymers, fabrication of wrapping foils and plastic sheets. Species, heat and momentum transfer play a prominent role in such processes. Polymeric sheets may be elongated in certain directions to enhance mechanical properties via doping with other materials and also thermal loading [15]. Non-Newtonian fluids arise in an extensive spectrum of chemical engineering systems including lubricants, medical linctus suspensions, detergents, foams, biotechnological liquids and so on. Rosali et al. [16] studied the stagnation point flow with a heat transfer toward a porous stretching/shrinking sheet. They found that the dual solution exist for shrinking case. Qasim [17] examined simultaneously the effects of heat and mass transfer on non-Newtonian Jeffreys viscoelastic fluid flow in the presence of heat source/sink. Mukhopadhyay [18] investigated the magnetized boundary layer flow with heat transfer through an exponentially stretching sheet in a thermally stratified medium. He observed that in the presence of thermal stratification effect, heat transfer rate rises, whereas the magnitude of the velocity profile diminishes for higher values of magnetic parameter. Khalili et al. [19] studied the unsteady stagnation point nanofluid flow with heat transfer through a stretching/shrinking sheet embedded in a porous medium under the effects of a magnetic field. They found that the dual solution domain rises due to an increment in magnetic parameter, permeability parameter and velocity ration while it remains constant for different values of solid volume fraction of nanoparticles. Further, they found that the permeability parameter has a more influence on a flow and heat transfer of nanofluid as compared to magnetic parameter. Later, Khalili et al. [20] considered the MHD effects on stagnation point nanofluid flow on a porous stretching/shrinking permeable plate. They considered three types of nanoparticles such as copper, alumina and titania with water as a base fluid. Further, they found that the skin friction coefficient and Nusselt number rise in all the three cases for higher values of nanoparticle volume fraction. Bhatti et al. [21] studied numerically the Maxwell fluid flow through a shrinking porous sheet using the successive linearization method.

In various high-temperature materials processing operations, thermal radiation heat transfer also plays an important role. The constitution of manufactured materials can be effectively manipulated with radiative flux. Thermal radiation is also significant in various other areas including rocket plume combustion, nuclear power plants, furnace operations, and reentry aero-thermodynamics. Seddeek and Abdelmeguid [22] studied the simultaneous effects of thermal radiation and thermal diffusivity on stretching surface flow with variable heat flux. Mukhopadhyay and Layek [23] investigated the impact of variable fluid viscosity and thermal radiation on free convection flow from a porous stretching sheet. They found that the suction parameter opposes the skin friction coefficient and enhances the heat transfer rate. However, for blowing case, the behavior is opposite. Moreover, they also observed that due to injection/suction fluid velocity increases/decreases at a particular point. Due to rise in thermal radiation parameter, temperature profile diminishes. Pal [24] analyzed the simultaneous effects of heat and mass transfer with thermal radiation and buoyancy force from a stretching surface. Mukhopadhyay [25] studied the unsteady mixed convection flow with heat transfer and thermal radiation through a porous media. Uddin et al. [26] simulated computationally the nonlinear magnetized slip flow from a stretching sheet with thermal radiative flux using with Maple quadrature.

Mabood et al. [27] numerically analyzed the boundary layer convection flow of nanofluid from a nonlinear stretching sheet. Daniel and Daniel [28] examined the thermal radiation effects on buoyancy-driven magnetic stagnation point flow through porous media. Bhatti and Rashidi [29] considered the simultaneous effects of thermal radiation and Soret thermo-diffusion on non-Newtonian viscoelastic nanofluid transport from a shrinking/stretching sheet. Recently, Akbar and Khan [30] explored the effects of thermal radiation and variable thermal conductivity on nanofluid stretching sheet flow with convective boundary conditions.

Magnetohydrodynamics (MHD) free convection flow is also an important area in modern engineering sciences. Recent developments in materials synthesis, electromagnetic flow control, magnetic levitation in metallurgy and electro-conductive polymers have stimulated significant interest in magneto-convective flow simulations. The resurge in renewable energy devices employing electromagnetic pumps and hydromagnetic generators has also mobilized substantial efforts in MHD heat transfer analysis. Makinde [31] investigated the combined influence of transverse magnetic field and thermal radiation on mixed convection flow with higher order chemical reaction through vertical porous media. Makinde [32] also analyzed studied magneto-convective heat and mass transfer from a moving vertical plate with surface convective boundary conditions. Ellahi and Hameed [33] studied numerically magnetohydrodynamic convection flow with nonlinear wall slip conditions. Akbar et al. [34] examined radiative flux effects on MHD stagnation point nanofluid flow from a stretching surface. Bég et al. [35] employed the PSPICE network simulation code to study the non-isothermal hydromagnetic boundary layer flow from a porous cone with pressure work and wall mass flux effects. Gaffar et al. [36] used a finite difference scheme to analyze the non-isothermal hydromagnetic flow of a tangent hyperbolic fluid from a vertical porous cone. Noor et al. [37] discussed the thermal radiation and heat absorption effects using a non-Newtonian fluid model through a vertical stretching sheet. They simultaneously used the shooting method with homotopy Pade solutions. Moreover, they found that the heat flux rises due to the increment in heat absorption and thermal radiation parameter. Halim et al. [38] considered the Maxwell fluid model with active and passive control flow in the presence of nanoparticles. They have also applied the shooting method to obtain the solution of the nonlinear equations. They found that the temperature profile in passive control model is lower as compared to the active control model. Moreover, they observed that Nusselt number, skin friction coefficient and Sherwood number diminish due to the increment in hydrodynamic slip parameter. Further, they noticed that the stagnation point parameter provides excellent heat transfer performance of nanofluid in the presence of both passive and active control models. Sheikholeslami and Bhatti [39] studied the influence of Coulomb force on forced convective heat transfer using Fe_3O_4–ethylene glycol nanofluid using control volume-based finite element method.

Relatively few studies of magnetohydrodynamic non-Newtonian convective heat and mass transfer have appeared utilizing a *non-Fourier* formulation for thermal conduction. In the present article, the objective is therefore to study the hydromagnetic forced convection heat and mass transfer in boundary layer flow of an upper-convected Maxwell fluid from a horizontal permeable stretching surface with the *non-Fourier Cattaneo–Christov heat flux model*. Additionally the collective effects of thermal radiation flux and chemical reaction are taken into account. This flow problem is relevant to polymeric materials processing operations in which thermal loading may be of the non-Fourier type [39–42]. The governing flow problem is modeled with the help of similarity transformation variables. The successive Taylor series linearization method (STSLM) [43–45] is used to solve the dimensionless boundary value problem. The physical influence of the emerging parameters on velocity, temperature and concentration profiles is elaborated with the aid of graphs. A numerical verification of the STSLM computations is also presented with an alternative numerical method as well as with existing published results. This paper is formulated in the following way. Section 1 relates the detailed background and introduction, and mathematical formulation of the problem is given in Sect. 2. Section 3 describes the numerical solution of the problem. Section 4 discusses validation with shooting quadrature and published literature. Section 5 contains numerical and graphical results of the problem.

2 Mathematical formulation

Consider the steady forced convective magnetohydrodynamic heat and mass transfer in boundary layer flow of an electrically-conducting, reactive non-Newtonian polymeric fluid (of the upper-convected Maxwell type) with thermal radiative flux, from a porous permeable stretching sheet at $y > 0$, as depicted in Fig. 1.

An external constant magnetic field, B_o, is applied in the transverse direction (y). The influence of induced magnetic is assumed to be negligible here due to small magnetic Reynolds number. The flow occurs on the origin of the stretching sheet due to the presence of two forces with opposite signs and equal values. The governing equations for the transport in the boundary layer may be written as [5, 6, 29]

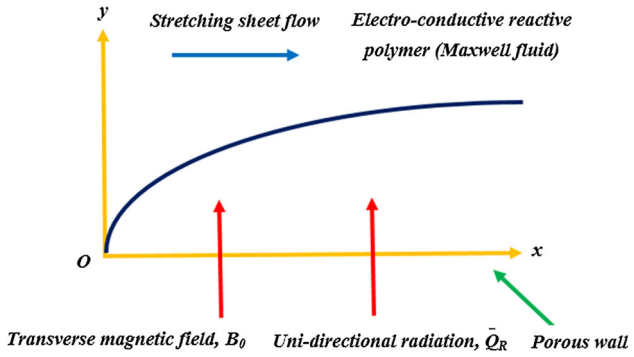

Fig. 1 Physical model for reactive radiative magnetized stretching heat and mass transfer

$$\frac{\partial \bar{u}}{\partial \bar{x}} + \frac{\partial \bar{v}}{\partial \bar{y}} = 0, \tag{1}$$

$$\bar{u}\frac{\partial \bar{u}}{\partial \bar{x}} + \bar{v}\frac{\partial \bar{u}}{\partial \bar{y}} = \nu\frac{\partial^2 \bar{u}}{\partial \bar{y}^2} - \Lambda\left[\bar{u}^2\frac{\partial^2 \bar{u}}{\partial \bar{x}^2} + \bar{v}^2\frac{\partial^2 \bar{u}}{\partial \bar{y}^2} + 2\bar{u}\bar{v}\frac{\partial^2 \bar{u}}{\partial \bar{y}\partial \bar{x}}\right] - \frac{\sigma B_0^2}{\rho}\left[\bar{u} + \Lambda\bar{v}\frac{\partial \bar{u}}{\partial \bar{y}}\right], \tag{2}$$

The *thermal boundary layer equation* using Cattaneo–Christov heat flux model in the presence of thermal radiation can be written in the following form [9, 12]:

$$\bar{u}\frac{\partial \bar{T}}{\partial \bar{x}} + \bar{v}\frac{\partial \bar{T}}{\partial \bar{y}} + \Lambda_1\left[\bar{u}\frac{\partial \bar{u}}{\partial \bar{x}}\frac{\partial \bar{T}}{\partial \bar{x}} + \bar{v}\frac{\partial \bar{v}}{\partial \bar{y}}\frac{\partial \bar{T}}{\partial \bar{y}} + \bar{u}\frac{\partial \bar{v}}{\partial \bar{x}}\frac{\partial \bar{T}}{\partial \bar{y}} + \bar{v}\frac{\partial \bar{u}}{\partial \bar{y}}\frac{\partial \bar{T}}{\partial \bar{x}} + 2\bar{u}\bar{v}\frac{\partial^2 \bar{T}}{\partial \bar{x}\partial \bar{y}} + \bar{u}^2\frac{\partial^2 \bar{T}}{\partial \bar{x}^2} + \bar{v}^2\frac{\partial^2 \bar{T}}{\partial \bar{y}^2}\right] = \bar{\alpha}\frac{\partial^2 \bar{T}}{\partial \bar{y}^2} - \frac{1}{\rho c_p}\frac{\partial \bar{Q}_R}{\partial \bar{y}}, \tag{3}$$

The species conservation boundary layer equation takes the form:

$$\bar{u}\frac{\partial \bar{C}}{\partial \bar{x}} + \bar{v}\frac{\partial \bar{C}}{\partial \bar{y}} = D\frac{\partial^2 \bar{C}}{\partial \bar{y}^2} - k_1(\bar{C} - \bar{C}_\infty). \tag{4}$$

where $\bar{u}$ and $\bar{v}$ are the velocity components in the $\bar{x}$ and $\bar{y}$ direction, respectively, Λ is the relaxation time, B_0 is the applied magnetic field, ν is the kinematic viscosity, ρ is the density of the fluid, σ is the electrical conductivity of the fluid, $\boldsymbol{q}$ is the heat flux, Λ_1 is the relaxation time of heat flux, $\bar{T}$ is the temperature, k is the thermal conductivity of the fluid, $\bar{V}$ is the velocity vector, respectively. Equation (3) can be reduced to Fourier's law by taking $\Lambda_1 = 0$.

In Eq. (3), the nonlinear radiative heat flux term may be rewritten as [21–26]:

$$\bar{Q}_r = -\frac{4\bar{\sigma}}{3k'}\frac{\partial \bar{T}^4}{\partial \bar{y}} = -\frac{16\bar{\sigma}\bar{T}^3}{3k'}\frac{\partial \bar{T}}{\partial \bar{y}}. \tag{5}$$

The boundary conditions at the wall and in the free stream are imposed as follows:

$$\bar{u} = a\bar{x},\ \bar{v} = -\bar{V}_s,\ \bar{T} = \bar{T}_w,\ \bar{C} = \bar{C}_w \quad \text{at } \bar{y} = 0, \tag{6}$$

$$\bar{u} \to \infty,\ \bar{T} = \bar{T}_\infty,\ \bar{C} = \bar{C}_\infty \quad \text{at } \bar{y} \to \infty. \tag{7}$$

In the above equations, a is constant, and $\bar{V}_s[>0]$ corresponds to a suction velocity, whereas $\bar{V}_s[<0]$ is associated with a blowing (injection) velocity at the wall, c_p is the specific heat, k' is the mean absorption coefficient, k_1 is the chemical reaction parameter, $\bar{\sigma}$ is the Stefan–Boltzmann constant and D is the coefficient of mass (species) diffusivity.

Introducing the similarity transformation variable ξ with the help of stream function, we have [9, 12]:

$$y = \xi\sqrt{\frac{\nu}{a}},\ \psi = x\sqrt{a\nu}f(\xi),\ \theta(\xi) = \frac{\bar{T} - \bar{T}_\infty}{\bar{T}_w - \bar{T}_\infty},\ \phi(\xi) = \frac{\bar{C} - \bar{C}_\infty}{\bar{C}_w - \bar{C}_\infty}. \tag{8}$$

The dimensional stream function is defined via the Cauchy–Riemann equations as:

$$\bar{u} = \frac{\partial \psi}{\partial \bar{y}}, \bar{v} = -\frac{\partial \psi}{\partial \bar{x}}. \tag{9}$$

Implementing the transformations defined in Eq. (8) into the momentum, thermal and species (concentration) boundary layer equations, i.e., Eqs. (2–4), the following system of ordinary differential equations emerges:

$$f''' - f'^2 - M^2 f' + \left(1 + \alpha M^2\right)ff'' - \alpha\left(f'''f^2 - 2f''f'f\right) = 0, \tag{10}$$

$$\left(\frac{1}{\mathrm{Pr}} + \frac{4}{3}R_d\right)\theta'' + f\theta' - \gamma\left(\theta' f' f + \theta'' f^2\right) = 0, \tag{11}$$

$$\frac{1}{\mathrm{Sc}}\phi' - \gamma_c\phi = f'\phi - f\phi'. \tag{12}$$

Their corresponding transformed boundary conditions are:

$$f = \lambda,\ f' = \mathrm{A},\ \theta = 1, \phi = 1 \quad \text{at } \xi = 0, \tag{13}$$

$$f' \to 0,\ \theta \to 1,\ \phi = 0 \quad \text{at } \xi \to \infty. \tag{14}$$

In the above equations, $\alpha = \Lambda a$ is the elasticity parameter, $M^2 = \sigma B_0^2/a\rho$ is the magnetic parameter, $\lambda = \frac{\bar{V}_s}{\sqrt{\nu a}}$ is the suction/injection parameter, $\mathrm{Pr} = \frac{\nu}{\bar{\alpha}}$ is the Prandtl number, $R_d = \frac{4\bar{\sigma}\bar{T}^3}{\rho c_p k'}$ is the conduction–radiation parameter, $A = \frac{b}{a}$ is the stretching parameter, $\mathrm{Sc} = \frac{\nu}{D}$ is the Schmidt number, γ_c is the chemical reaction parameter and $\gamma = \Lambda_1 a$ is the modified Deborah number with respect to relaxation time of heat flux (i.e., *non-Fourier* Deborah number). The physical quantities of interest, i.e., engineering design parameters of relevance to materials processing are skin friction coefficient, local Nusselt number and Sherwood number. These are defined in dimensionless form as [29]:

$$C_{fx} = f''(0),\ \mathrm{Nu}_x = -\left(1+\frac{4}{3}R_d\right)\theta'(0),\ \mathrm{Sh}_x = -\phi'(0). \tag{15}$$

3 STSLM numerical solutions

The nonlinear boundary value problem defined by the reduced momentum, energy and thermal boundary layer equations together with the boundary conditions, i.e., Eqs. (10–14), may be solved by a variety of computational techniques. In the present study, we elect to use the powerful successive Taylor series linearization method (STSLM) employing Chebyshev interpolating polynomials and Gauss–Lobatto collocation. In order to apply STSLM, let us define

$$f(\xi) = f_I(\xi) + \sum_{N=0}^{I-1} f_N(\xi), \quad I = 1,2,3,\ldots, \tag{16}$$

where f_I are unknown functions which are obtained by iteratively solving the linearized version of the governing equation and assuming that $f_I(0 \le N \le I-1)$ are known from previous iterations. Our algorithm starts with an initial approximation, f_0, which satisfy the given boundary conditions in Eq. (13) according to STSLM. Equation (10) can be written in the following form

$$L(f,f',f'',f''') + N(f,f',f'',f''') = 0, \tag{17}$$

where L and N are linear nonlinear part.

$$L(f,f',f'',f''') = f''' - M^2 f', \tag{18}$$

$$N(f,f',f'',f''') = \left(1+\alpha M^2\right)f''f - \alpha\left(f'''f^2 - 2ff'f''\right) - f'^2. \tag{19}$$

Using Eqs. (10) and (16), we have

$$f_I''' + A_{0,I-1}f_I''' + A_{1,i-1}f_I'' + A_{2,i-1}f_I' + A_{3,i-1}f_I - M^2 f_I' = R_{I-1}(\xi). \tag{20}$$

The corresponding boundary conditions become:

$$f_I(0) = 0, f_I'(0) = 0, f_I'(\infty) = 0, \tag{21}$$

where $A_{0,I-1}, A_{1,I-1}, A_{2,I-1}, A_{3,I-1}$ and R_{I-1} can be find using routine calculations. The initial guess is chosen in the following form, which satisfies all the corresponding boundary conditions, i.e.,

$$f_0(\xi) = \lambda - \mathrm{A}\left(e^{-\xi} - 1\right). \tag{22}$$

With the help of the initial approximation, Eq. (20) can be solve iteratively to obtain the subsequent solution for $f_N(N \ge 1)$. The ith-order approximation solutions for $f(\xi)$ can be written as:

$$f(\xi) \approx \sum_{N=0}^{I} f_N(\xi). \tag{23}$$

The right-hand side of Eq. (20) for $i = 1, 2, 3,\ldots$ and furthermore the coefficient of each parameter can be obtained from the previous iterations. We have applied the Chebyshev spectral collocation method to obtain the solution for Eq. (20). This method involves approximating the unknown functions using Chebyshev interpolating polynomials defined on the interval $[-1, 1]$ by:

$$C_K(\eta) = \cos\left[K\cos^{-1}(\xi)\right]. \tag{24}$$

For the application of this method, the physical infinite region is transformed into the finite region, i.e., $[0,\infty) \to [-1,1]$ with the help of a domain truncation method, while the solution is obtained in the interval $[0, l]$ instead of $[0, \infty)$. This leads to the following mapping:

$$\frac{\xi}{l} = \frac{\eta+1}{2}, \quad -1 \le \eta \le 1, \tag{25}$$

Here l is a scaling parameter which helps to invoke the boundary conditions defined on infinity. To define the Chebyshev nodes in $[-1, 1]$, we have applied Gauss–Lobatto collocation points. The variable f_I is analyzed using an interpolating polynomial at each collocation point with the help of truncated Chebyshev series in the following form:

$$f_I(\eta) = \sum_{K=0}^{i} f_I(\eta_K)C_K(\eta_J), \quad J = 0,1\ldots i, \tag{26}$$

where C_K is the Kth Chebyshev polynomial. At the collocation points, the derivatives of the variables can be written as:

$$\frac{\mathrm{d}^p f_I}{\mathrm{d}\xi^p} = \sum_{K=0}^{i} \boldsymbol{D}_{\boldsymbol{KJ}}^{\boldsymbol{p}} f_I(\eta_K), \quad J = 0,1\ldots i, \tag{27}$$

where p is the order of differential matrix and $\boldsymbol{D} = \frac{2}{l}\mathcal{D}$ in which $\mathcal{D}$ is a Chebyshev spectral differentiation matrix. Using Eqs. (26) and (27) in Eqs. (20) and (21), we have:

$$A_{I-1}G_I = \phi_{I-1}. \tag{28}$$

Subject to

$$f_I(\eta_i) = 0, \quad \sum_{K=0}^{i} \boldsymbol{D}_{\boldsymbol{iK}} f_I(\eta_K) = 0, \quad \sum_{K=0}^{i} \boldsymbol{D}_{\boldsymbol{0K}} f_I(\eta_K) = 0, \tag{29}$$

where

$$A_{I-1} = \left[\boldsymbol{I} + A_{0,I-1}\right]\boldsymbol{D}^3 + A_{1,I-1}\boldsymbol{D}^2 + \left[A_{2,I-1} - M^2\boldsymbol{I}\right]\boldsymbol{D} + A_{3,I-1,} \tag{30}$$

$$G_I = [f_I(\eta_0), f_I(\eta_1), \ldots f_I(\eta_i)]^t, \tag{31}$$

$$\phi_{I-1} = [\phi_{I-1}(\eta_0), \phi_{I-1}(\eta_1), \ldots \phi_{I-1}(\eta_i)]^t. \tag{32}$$

In the above equations, t is transpose, $A_{K,I-1}$ ($K = 0, 1, 2, 3$) is a diagonal matrix of size $(i+1) \times (i+1)$ and $\boldsymbol{I}$ is identity matrix of size $(i+1) \times (i+1)$. The boundary condition $f_I(\eta_i) = 0$ is employed by removing the last column and last row of A_{I-1} and by deleting the last rows of G_I and ϕ_{I-1}. Then the boundary conditions in Eq. (29) are imposed to the last and first row of A_{I-1}. The last and first rows of ϕ_{I-1} and G_I are set to zero. The solution for $f_I(\eta_1)$, $f_I(\eta_2)$, …, $f_I(\eta_{i-1})$ is iteratively obtained after solving:

$$G_I = A_{I-1}^{-1}\phi_{I-1}. \tag{33}$$

Once the solutions are obtained, we can apply directly the Chebyshev pseudo-spectral method to Eq. (11) and Eqs. (12–13), leading to:

$$\mathcal{B}\mathcal{H} = \mathcal{S}. \tag{34}$$

With the relevant boundary conditions

$$\theta(\eta_i) = \phi(\eta_i) = 1, \theta(\eta_0) = \phi(\eta_0) = 0. \tag{35}$$

Here $\mathcal{B}$ is the linear differential equation, $\mathcal{H}$ is a column vector and $\mathcal{S}$ is a vector of zeros. The corresponding boundary conditions in Eq. (35) are replaced in the first and last rows of $\mathcal{S}$ and $\mathcal{B}$, respectively.

4 Validation of STSLM solutions

To verify the accuracy of the successive Taylor series linearization method (STSLM), a numerical comparison is presented with shooting method using the symbolic computational software Mathematica. The value of l in STSLM is considered to be $l = 15$, and the number of collocation points is $i = 60$. These values are found to be appropriate for the present flow and are in excellent agreement with the results obtained by shooting method. STSLM is computationally more accurate and efficient as compared to other similar methods since it gives more accurate results when a governing problem is directly solved. Table 1 shows the numerical results of skin friction coefficient and Nusselt number for a range of parameter values for both STSLM and shooting method, and very good agreement is achieved. Confidence in the STSLM solutions is therefore justifiably high. Table 2 shows the numerical comparison of skin friction coefficient with existing published studies [46–49], i.e., Abel et al. [46], Megahed [47], Sadeghy et al. [48] and Mukhopadhyay [49] by taking $M = \alpha = \lambda = 0$ as a special case of our study.

5 Numerical results and discussion

In this section, numerical results are presented in Figs. 2, 3, 4, 5, 6, 7, 8, 9 and 10, in order to study the influence of the key physical parameters, i.e., magnetic parameter (M), elasticity parameter (α), suction/injection parameter (λ), stretching parameter (A), Prandtl number (Pr), conduction–radiation parameter (R_d) and non-Fourier Deborah number (γ) on the heat, momentum and species characteristics in the regime.

Figure 2a, b depicts the variation of elasticity parameter (α) on both velocity components, i.e., u component and v component. These figures elucidate that greater elasticity parameter (α) causes a marked reduction in the velocity profiles, i.e., stronger elastic effects decelerate the boundary layer flow and increase momentum boundary layer thickness. α is directly proportional to the relaxation time (Λ) of the polymer (viscoelastic fluid). An elasticoviscous material such as the upper-convected Maxwell (UCM) fluid has a fading memory; it retains information of recent deformation. With greater relaxation time, the elastic effects dominate rather than the viscous effects. This results in retardation in the flow with higher values of α. The case of $\alpha = 0$ *corresponds to purely viscous flow (vanishing elastic effect),* and clearly for this case, the velocity components are maximized, i.e., there is flow acceleration. We further note that the u-velocity component decays monotonically from the wall into the free stream, whereas the v component grows from the wall to the free stream, irrespective of the value of the elasticity parameter.

Figure 3a, b illustrates the impact of magnetic body force parameter (M) on both velocity components, i.e., u component and v component. The transverse magnetic field (imposed in the y-direction, i.e., ξ-direction) generates an impeding Lorentz magnetohydrodynamic body force along the x-direction. Magnetic body force terms arise twice in the momentum conservation Eq. (12), i.e., $-M^2 f'$ and $(\alpha M^2) f f''$. This creates a significant resistance to the boundary layer flow and induces a deceleration in both u- and v-velocity component. The case of $M = 0$ corresponds to electrically nonconducting polymer flow in which magnetohydrodynamic effects vanish. Physically, as M increases, the Lorentz force also increases and this produces significant control of the boundary layer flow and substantial retardation which may be exploited in materials processing operations. The trends in the computations are also qualitatively similar to the results obtained by Alizadeh-Pahlavan et al. [50]. Again there is a consistent decay in the u-velocity component with increasing transverse

Table 1 Numerical comparison of STSLM and shooting method for skin friction, Nusselt number and Sherwood number for different parametric values

	STSLM			Shooting method		
	C_{fx}	Nu_x	Sh_x	C_{fx}	Nu_x	Sh_x
M						
0.5	−0.97774	0.52425	1.53471	−0.97774	0.52425	1.53471
1	−1.26542	0.35126	1.48605	−1.26542	0.35126	1.48605
1.5	−1.64096	0.19140	1.42749	−1.64096	0.19140	1.42749
α						
0.5	−0.97357	0.48426	1.52839	−0.97357	0.48426	1.52839
1	−0.96262	0.43875	1.52160	−0.96262	0.43875	1.52160
1.5	−0.94637	0.39867	1.51583	−0.94637	0.39867	1.51583
λ						
−0.4	−0.92921	0.48116	1.44940	−0.92921	0.48116	1.44940
0	−1.14520	0.78738	1.82200	−1.14520	0.78738	1.82200
0.3	−1.35238	1.35044	2.15506	−1.35238	1.35044	2.15506
A						
0.5	−0.36251	0.21555	1.19382	−0.36251	0.20567	1.19382
0.8	−0.70663	0.40449	1.40675	−0.64386	0.34924	1.40675
0.9	−0.83827	0.46505	1.47193	−0.83827	0.43176	1.47193
Pr						
4.5		0.59139			0.59139	
5.5		0.62167			0.62167	
6.8		0.65119			0.65119	
R_d						
0.4		0.50585			0.50585	
0.6		0.49786			0.49786	
0.8		0.49445			0.49445	
γ						
0.3		0.49398			0.49398	
0.5		0.51373			0.51373	
0.7		0.53524			0.53524	
γ_c						
0			1.19097			1.19097
0.6			1.59344			1.59344
1.2			1.90672			1.90672
Sc						
1.2			1.20272			1.20272
1.6			1.38239			1.38239
2.0			1.53471			1.53471

Table 2 Numerical comparison of skin friction coefficient with existing published results $M = \alpha = 0$

	Abel et al. [46]	Megahed [47]	Sadeghy et al. [48]	Mukhopadhyay [49]	Present results
C_{fx}	−0.999962	−0.999978	−1.000000	−0.999996	−1.000000

coordinate (ξ), whereas the v-velocity component grows with increasing transverse coordinate (ξ). Effectively momentum boundary layer thickness is increased with stronger magnetic parameter (M) values.

Figure 4a, b elucidates the behavior of suction/injection parameter (λ) on both u component and v component of velocity. Figure 4a indicates that an enhancement in suction ($\lambda > 0$) causes a marked reduction in the u component

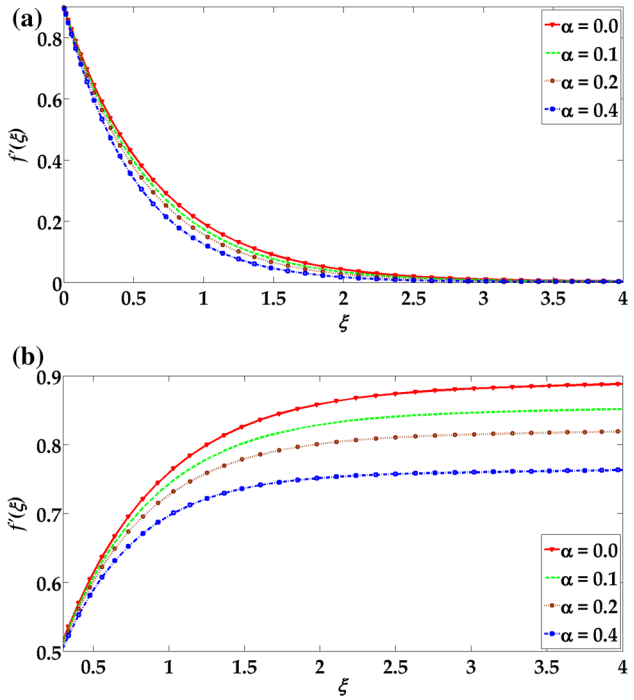

Fig. 2 Effect of elasticity parameter α on velocity profile. **a** *u* component, **b** *v* component

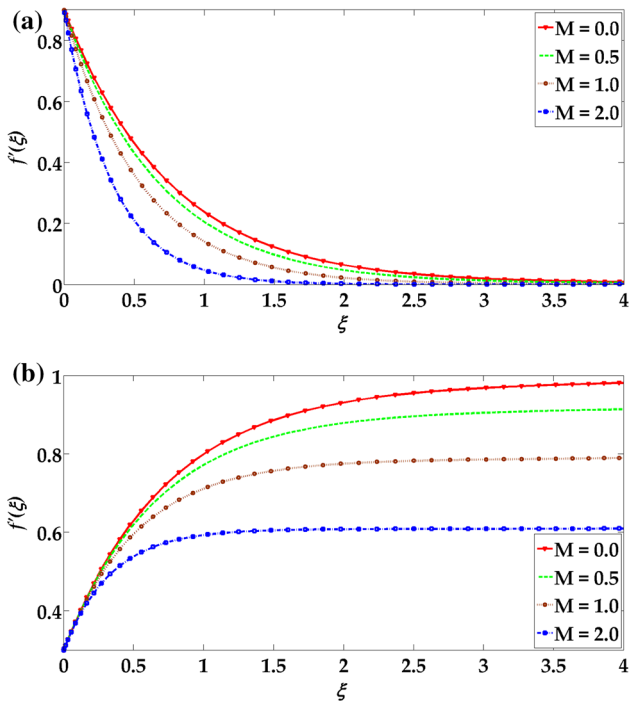

Fig. 3 Effect of magnetic parameter *M* on velocity profile. **a** *u* component, **b** *v* component

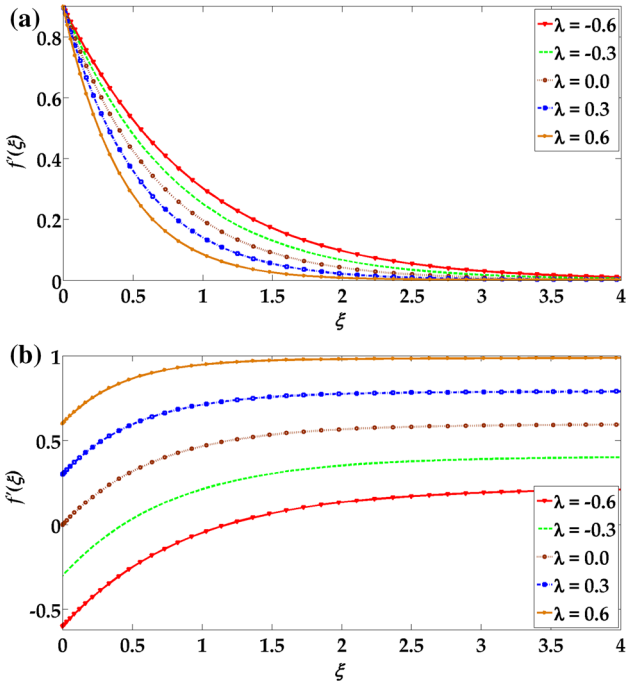

Fig. 4 Effect of suction/injection parameter λ on velocity profile. **a** *u* component, **b** *v* component

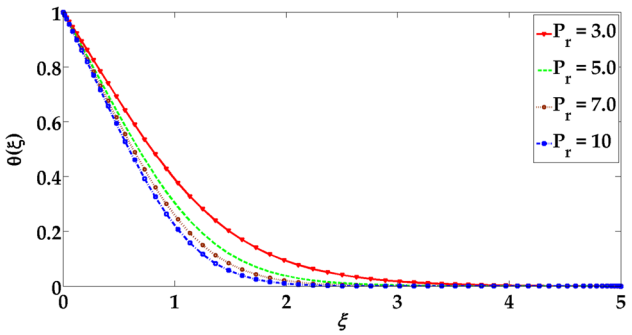

Fig. 5 Effect of Prandtl number Pr on temperature profile

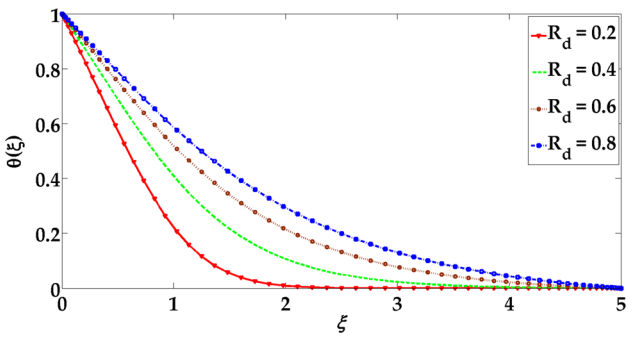

Fig. 6 Effect of radiation parameter R_d on temperature profile

of velocity. Greater suction induces stronger adherence of the boundary layer to the wall in the stretching sheet regime. This decelerates the flow and increases momentum boundary layer thickness. Conversely increasing injection effect ($\lambda < 0$) induces the opposite effect. Blowing (injection) of fluid through the porous wall enhances momentum transfer which accelerates the *u*-velocity component strongly and decreases momentum (hydrodynamic)

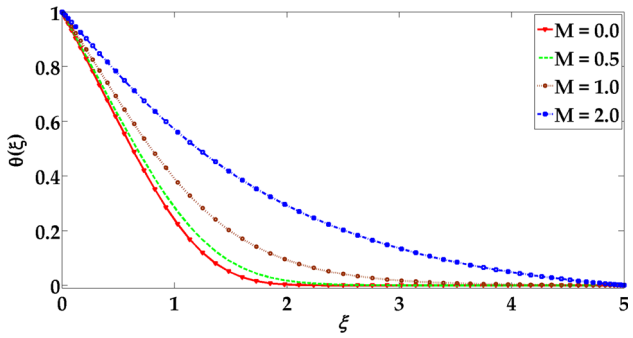

Fig. 7 Effect of magnetic parameter M on temperature profile

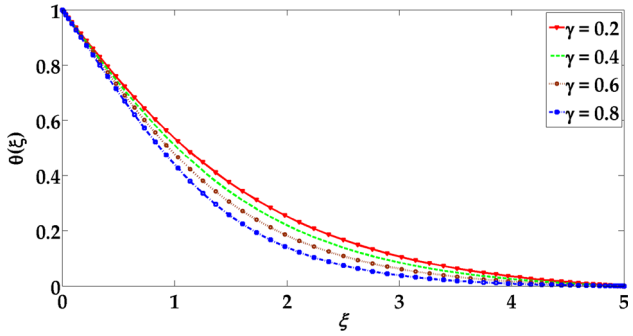

Fig. 8 Effect of Deborah number γ on temperature profile

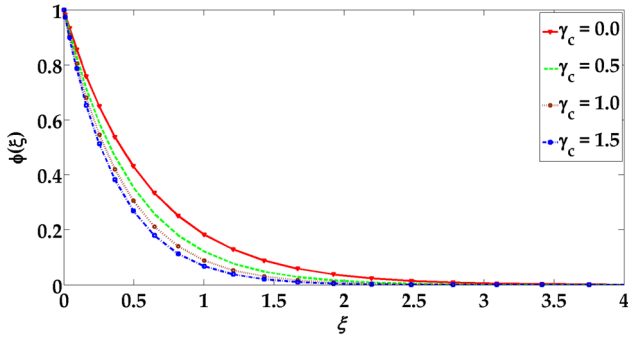

Fig. 9 Effect of chemical reaction γ_c on concentration profile

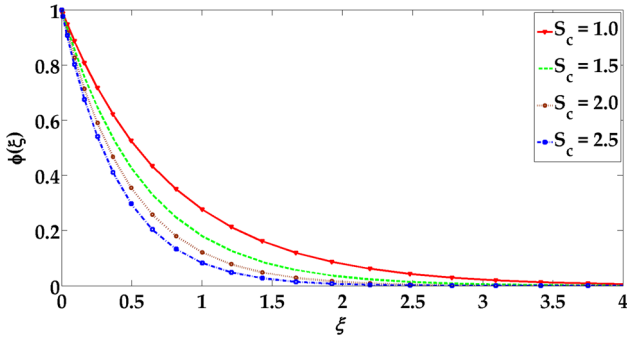

Fig. 10 Effect of Schmidt number Sc on concentration profile

boundary layer thickness. These results agree with the patterns computed in other studies, e.g., Mukhopadhyay [25] and Uddin et al. [26]. Figure 3b indicates that the opposite response is computed for the effects of suction/injection parameter on v component of velocity. Greater injection ($\lambda < 0$) clearly retards the v-component velocity (increases momentum boundary layer thickness), whereas greater suction (>0), significantly accelerates the v-component (decreases momentum boundary layer thickness). Furthermore whereas u component is consistently zero at the wall (irrespective of injection or suction at the wall), the v component is generally nonzero at the wall. The wall value of v-component velocity is greatest with strongest suction.

Figures 5, 6, 7 and 8 show the behavior of temperature profile with respective variation in Prandtl number Pr, radiation parameter R_d, non-Fourier Deborah number γ and Hartmann number M. Figure 5 shows that an increment in Prandtl number Pr progressively decreases the temperature profile and therefore reduces thermal boundary layer thickness. The higher Prandtl number values studied, i.e., $\mathrm{Pr} > 1$ are representative of polymeric non-Newtonian fluids. The Prandtl number defines the ratio between momentum diffusivity and thermal diffusivity. Higher values of Prandtl number are associated with lower thermal diffusivity. Furthermore Prandtl number is inversely proportional to thermal conductivity. Polymers possess lower thermal conductivities and therefore higher Prandtl numbers than, for example, liquid metals. The decrease in thermal conductivity with greater Prandtl number results in a strong decrease in temperatures in the boundary layer.

Figure 6 shows that with increase in conduction–radiation parameter (R_d) consistently enhances temperature magnitudes and thereby elevates thermal boundary layer thickness. Physically, when the radiation parameter R_d is high, the radiative flux energizes the polymeric flow which adds thermal energy to the regime. This boosts the temperatures in the boundary layer. For low values of R_d, thermal conduction heat transfer is more dominant compared with thermal radiation, and this results in decreased temperatures.

Figure 7 shows that when the magnetic parameter (M) increases, temperature magnitudes are strongly enhanced. The supplementary work expended in dragging the polymer against the action of the magnetic field (Fig. 3a, b) is dissipated as thermal energy, i.e., heat. This energizes the boundary layer and also leads to an increase in thermal boundary layer thickness. We further note that the smooth profiles in the free stream in the plot (and indeed also in all other figures) indicate that a sufficiently high value for infinity is imposed in the STSLM solutions.

Figure 8 shows that for higher values of non-Fourier Deborah number (γ), there is a marked decrease in temperatures throughout the boundary layer and an associated reduction in thermal boundary layer thickness. The modified Deborah number γ embodies the supplementary effect

due to heat flux relaxation time which is captured in the non-Fourier model and is absent in the classical Fourier model. The *non-Fourier* Cattaneo–Christov heat flux model can be reduced to simple Fourier law of heat conduction by taking $\gamma = 0$. Fluids with shorter heat flux relaxation time are associated with higher temperatures, while the fluid with longer heat flux is associated with lower temperature. With increasing Deborah number (γ), a longer heat flux is achieved which causes a *higher rate of heat transfer from the fluid to the wall* and therefore a lower temperature within the fluid, i.e., heat is depleted from the fluid. This also results in a decrement in thermal boundary layer thickness.

Figures 9 and 10 show the response in concentration profile with chemical reaction parameter (γ_c) and Schmidt number (Sc). Figure 9 demonstrates that increasing chemical reaction parameter (γ_c) causes a marked reduction in the concentration profile. The reaction term in the dimensionless concentration boundary layer Eq. (14), i.e., $-\gamma_c\phi$ is based on a first-order irreversible chemical reaction which takes place both in the bulk of the fluid (homogeneous) as well as at the wall which is assumed to be catalytic to chemical reaction. Although chemical reactions generally fall into one of two categories, i.e., homogenous or heterogenous, the former is of interest in the present study. Homogenous chemical reactions take place uniformly throughout a given phase and exert a similar influence to an *internal source of heat generation*. We consider the destructive type of homogenous chemical reaction. Increasing the chemical reaction parameter (γ_c) produces a decrease in velocity. The momentum boundary layer thickness is therefore increased substantially with greater chemical reaction effect. It is noticed that concentration distributions decrease when the chemical reaction increases. Physically, for a destructive case, chemical reaction takes place and progressively destroys the original species diffusing in the polymeric viscoelastic fluid. This, in turn, suppresses molecular diffusion of the remaining species which leads to a fall in concentration magnitudes and a decrease in concentration boundary layer thickness.

Figure 10 reveals that an increment in Schmidt number (Sc) decreases the concentration magnitudes strongly, i.e., reduces ϕ values. The Schmidt number embodies the ratio of the momentum to the mass diffusivity, i.e., $\mathrm{Sc} = \nu/D$. The Schmidt number therefore quantifies the relative effectiveness of momentum and mass transport by diffusion in the hydrodynamic (velocity) and concentration (species) boundary layers. For $\mathrm{Sc} > 1$, momentum diffusion rate *exceeds* the species diffusion rate. The opposite applies for $\mathrm{Sc} < 1$. For $\mathrm{Sc} = 1$, both momentum and concentration (species) boundary layers will have the same thickness, and diffusivity rates will be equal. It is observed that as the Schmidt number increases, species

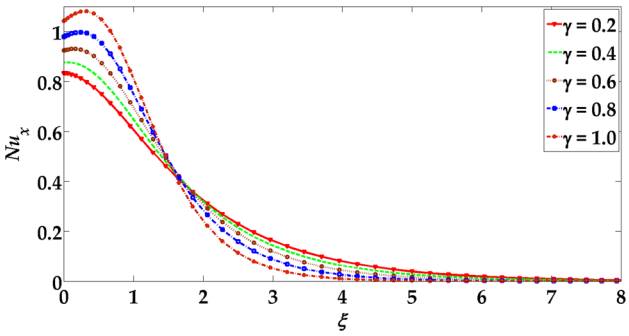

Fig. 11 Effect of Deborah number γ on Nusselt number

(concentration) profiles gradually decrease. Smaller values of Scare equivalent to increasing the chemical molecular diffusivity and vice versa for larger values of Sc. Concentration boundary layer thickness is therefore significantly reduced with greater Schmidt number. Figure 11 reveals the effects of Deborah number on Nusselt number profile.

6 Conclusions

In this article, a mathematical model has been developed to investigate the influence of chemical reaction, thermal radiation and wall mass flux on magnetohydrodynamic heat and mass transfer in the flow of an upper-convected Maxwell fluid from a permeable stretching sheet under the effects of constant magnetic field. The non-Fourier Cattaneo–Christov heat flux model has been implemented (the Cattaneo–Christov heat flux model can be reduced to the classical Fourier law of heat conduction when Deborah number $\gamma = 0$). Numerical solutions are presented for the transformed, dimensionless boundary value problem with appropriate wall and free stream conditions, using the successive Taylor series linearization method (STSLM) which utilizes both Chebyshev interpolating polynomials and Gauss–Lobatto collocation. Validation of STSLM computations has also been included using a Mathematica-based shooting algorithm and also published results from the literature. The major conclusions from the present computations may be summarized as follows:

1. Both (u,v) velocity components diminish due to the increment in elasticity parameter.
2. Both (u,v) velocity components are decreased with an increase in magnetic parameter.
3. When the suction/injection parameter increases, then the velocity of the fluid decreases markedly along u component of velocity, whereas the converse behavior is computed for the v component of velocity.

4. Higher values of radiation and magnetic parameter induce a significant increase in temperature profile and thermal boundary layer thickness.
5. Thermal boundary layer thickness and temperature magnitudes decrease for large values of non-Fourier Deborah number and Prandtl number.
6. Concentration magnitudes are suppressed with large values of Schmidt number and chemical reaction parameter.

The present study has ignored *magnetic induction* effects which are invoked at higher magnetic Reynolds number. These are currently being investigated.

Compliance with ethical standards

Conflict of interest The authors declare no conflict of interest.

References

1. Fourier JBJ (1822) Theorie analytique de la chaleur. English translation: The analytic theory of heat (1878). Firman Didot, Paris
2. Cattaneo C (1948) Sulla conduzione del calore. Atti Semin Mat Fis della Università di Modena 3:3
3. Christov CI (2009) On frame indifferent formulation of the Maxwell–Cattaneo model of finite-speed heat conduction. Mech Res Commun 36(4):481–486
4. Ostoja-Starzewski M (2009) A derivation of the Maxwell–Cattaneo equation from the free energy and dissipation potentials. Int J Eng Sci 47(7):807–810
5. Tibullo V, Zampoli V (2011) A uniqueness result for the Cattaneo–Christov heat conduction model applied to incompressible fluids. Mech Res Commun 38(1):77–79
6. Straughan B (2010) Thermal convection with the Cattaneo–Christov model. Int J Heat Mass Transf 53(1):95–98
7. Haddad SAM (2014) Thermal instability in Brinkman porous media with Cattaneo–Christov heat flux. Int J Heat Mass Transf 68:659–668
8. Ciarletta M, Straughan B (2010) Uniqueness and structural stability for the Cattaneo–Christov equations. Mech Res Commun 37(5):445–447
9. Al-Qahtani H, Yilbas BS (2010) The closed form solutions for Cattaneo and stress equations due to step input pulse heating. Phys B 405(18):3869–3874
10. Papanicolaou NC, Christov CI, Jordan PM (2011) The influence of thermal relaxation on the oscillatory properties of two-gradient convection in a vertical slot. Eur J Mech B/Fluids 30(1):68–75
11. Han S, Zheng L, Li C, Zhang X (2014) Coupled flow and heat transfer in viscoelastic fluid with Cattaneo–Christov heat flux model. Appl Math Lett 38:87–93
12. Mustafa M (2015) Cattaneo–Christov heat flux model for rotating flow and heat transfer of upper-convected Maxwell fluid. AIP Adv 5(4):047109
13. Bissell JJ (2015) On oscillatory convection with the Cattaneo-Christov hyperbolic heat-flow model. Proc R Soc A 471:20140845
14. Nadeem S, Haq RU, Akbar NS, Lee C, Khan ZH (2013) Numerical study of boundary layer flow and heat transfer of Oldroyd-B nanofluid towards a stretching sheet. PLoS ONE 8(8):e69811
15. Kumaran V, Ramanaiah G (1996) A note on the flow over a stretching sheet. Acta Mech 116:229–233
16. Rosali H, Ishak A, Pop I (2011) Stagnation point flow and heat transfer over a stretching/shrinking sheet in a porous medium. Int Commun Heat Mass Transf 38:1029–1032
17. Qasim M (2013) Heat and mass transfer in a Jeffrey fluid over a stretching sheet with heat source/sink. Alex Eng J 52:571–575
18. Mukhopadhyay S (2013) MHD boundary layer flow and heat transfer over an exponentially stretching sheet embedded in a thermally stratified medium. Alex Eng J 52:259–265
19. Khalili S, Dinarvand S, Hosseini R, Tamim H, Pop I (2014) Unsteady MHD flow and heat transfer near stagnation point over a stretching/shrinking sheet in porous medium filled with a nanofluid. Chin Phys B 23:048203
20. Khalili S, Dinarvand S, Hosseini R, Saber M, Pop I (2014) Magnetohydrodynamic stagnation point flow toward stretching/shrinking permeable plate in porous medium filled with a nanofluid. Proc Inst Mech Eng E J Process Mech Eng 228:309–319
21. Bhatti MM, Shahid A, Rashidi MM (2016) Numerical simulation of fluid flow over a shrinking porous sheet by successive linearization method. Alex Eng J 55(1):51–56
22. Seddeek MA, Abdelmeguid MS (2006) Effects of radiation and thermal diffusivity on heat transfer over a stretching surface with variable heat flux. Phys Lett A 348(3):172–179
23. Mukhopadhyay S, Layek GC (2008) Effects of thermal radiation and variable fluid viscosity on free convective flow and heat transfer past a porous stretching surface. Int J Heat Mass Transf 51(9):2167–2178
24. Pal D (2009) Heat and mass transfer in stagnation-point flow towards a stretching surface in the presence of buoyancy force and thermal radiation. Meccanica 44(2):145–158
25. Mukhopadhyay S (2009) Effect of thermal radiation on unsteady mixed convection flow and heat transfer over a porous stretching surface in porous medium. Int J Heat Mass Transf 52(13):3261–3265
26. Uddin MJ, Bég OA, Uddin MN (2016) Energy conversion, conjugate conduction, magneto-convection, diffusion and non-linear radiation over a moving non-linearly extruding permeable stretching sheet with slip, thermal and mass convective boundary conditions. Energy 115:1119–1129
27. Mabood F, Khan WA, Ismail AM (2015) MHD boundary layer flow and heat transfer of nanofluids over a nonlinear stretching sheet: a numerical study. J Magn Magn Mater 374:569–576
28. Daniel YS, Daniel SK (2015) Effects of buoyancy and thermal radiation on MHD flow over a stretching porous sheet using homotopy analysis method. Alex Eng J 54(3):705–712
29. Bhatti MM, Rashidi MM (2016) Effects of thermo-diffusion and thermal radiation on Williamson nanofluid over a porous shrinking/stretching sheet. J Mol Liq 221(2016):567–573
30. Akbar NS, Khan ZH (2016) Effect of variable thermal conductivity and thermal radiation with CNTS suspended nanofluid over a stretching sheet with convective slip boundary conditions: Numerical study. J Mol Liq 222:279–286
31. Makinde OD (2010) MHD mixed-convection interaction with thermal radiation and nth order chemical reaction past a vertical porous plate embedded in a porous medium. Chem Eng Commun 198(4):590–608
32. Makinde OD (2010) On MHD heat and mass transfer over a moving vertical plate with a convective surface boundary condition. Can J Chem Eng 88(6):983–990
33. Ellahi R, Hameed M (2012) Numerical analysis of steady non-Newtonian flows with heat transfer analysis, MHD and nonlinear slip effects. Int J Numer Methods Heat Fluid Flow 22(1):24–38
34. Akbar NS, Nadeem S, Haq RU, Khan ZH (2013) Radiation effects on MHD stagnation point flow of nanofluid towards a

stretching surface with convective boundary condition. Chin J Aeronaut 26(6):1389–1397
35. Bég OA, Zueco J, Bég TA, Kadir A, Khan UF (2016) Network electro-thermal simulation of non-isothermal magnetohydrodynamic heat transfer from a transpiring cone with pressure work effects. Int J Appl Comput Math USA. doi:10.1007/s40819-016-0192-5
36. Gaffar SA, Ramachandra Prasad V, Keshava Reddy S, Bég OA (2016) Magnetohydrodynamic free convection boundary layer flow of non-Newtonian tangent hyperbolic fluid from a vertical permeable cone with variable surface temperature. J Braz Soc Mech Sci Eng. doi:10.1007/s40430-016-0611-x
37. Noor NFM, Ul Haq R, Abbasbandy S, Hashim I (2016) Heat flux performance in a porous medium embedded Maxwell fluid flow over a vertically stretched plate due to heat absorption. J Nonlinear Sci Appl 9(5):2986–3001
38. Halim NA, Haq RU, Noor NFM (2016) Active and passive controls of nanoparticles in Maxwell stagnation point flow over a slipped stretched surface. Meccanica 1–13. doi:10.1007/s11012-016-0517-9
39. Sheikholeslami M, Bhatti MM (2017) Active method for nanofluid heat transfer enhancement by means of EHD. Int J Heat Mass Transf 109:115–122
40. Ocone R, Astarita G (1987) Continuous and discontinuous models for transport phenomena in polymers. AIChemE J 33:423–435
41. Zhe Z, Dengying L (2000) The research progress of the non-Fourier heat conduction. Adv Mech 30:123–141
42. Huilgol RR (1992) A theoretical and numerical study of non-Fourier effects in viscometric and extensional flow of an incompressible simple fluid. J Non-Newtonian Fluid Mech 43:83–102
43. Motsa SS, Hayat T, Aldossary OM (2012) MHD flow of upper-convected Maxwell fluid over porous stretching sheet using successive Taylor series linearization method. Appl Math Mech 33(8):975–990
44. Bhatti MM, Rashidi MM, Pop I (2017) Entropy generation with nonlinear heat and mass transfer on MHD boundary layer over a moving surface using SLM. Nonlinear Eng. doi:10.1515/nleng-2016-0021
45. Bhatti MM, Abbas T, Rashidi MM (2017) Entropy generation as a practical tool of optimisation for non-Newtonian nanofluid flow through a permeable stretching surface using SLM. J Comput Des Eng 4(1):21–28
46. Abel MS, Tawade JV, Nandeppanavar MM (2012) MHD flow and heat transfer for the upper-convected Maxwell fluid over a stretching sheet. Meccanica 47(2):385–393
47. Megahed AM (2013) Variable fluid properties and variable heat flux effects on the flow and heat transfer in a non-Newtonian Maxwell fluid over an unsteady stretching sheet with slip velocity. Chin Phys B 22(9):094701
48. Sadeghy K, Hajibeygi H, Taghavi SM (2006) Stagnation-point flow of upper-convected Maxwell fluids. Int J Non-Linear Mech 41(10):1242–1247
49. Mukhopadhyay S (2012) Heat transfer analysis of the unsteady flow of a Maxwell fluid over a stretching surface in the presence of a heat source/sink. Chin Phys Lett 29(5):054703
50. Alizadeh-Pahlavan A, Aliakbar V, Vakili-Farahani F, Sadeghy K (2009) MHD flows of UCM fluids above porous stretching sheets using two-auxiliary-parameter homotopy analysis method. Commun Nonlinear Sci Numer Simul 14:473–488